Article

The Reaction Mechanism for the Hydrogen Evolution Reaction on the Basal Plane Sulfur Vacancy Site of MoS2 Using Grand Canonical Potential Kinetics

Yufeng Huang, Robert J. Nielsen, and William A. Goddard

J. Am. Chem. Soc., **Just Accepted Manuscript** • DOI: 10.1021/jacs.8b10016 • Publication Date (Web): 08 Nov 2018

The Reaction Mechanism for the Hydrogen Evolution Reaction on the Basal Plane Sulfur Vacancy Site of MoS_2 Using Grand Canonical Potential Kinetics

Yufeng Huang, Robert J. Nielsen, William A. Goddard III*

Materials and Process Simulation Center and Joint Center for Artificial Photosynthesis, California Institute of Technology, Pasadena, CA 91125, U.S.A.

KEYWORDS: Electrochemistry, Grand Canonical Potential, Hydrogen Evolution Reaction, Molybdenum Disulfide

ABSTRACT: We develop the grand canonical potential kinetics (GCP-K) formulation based on thermodynamics from quantum mechanics calculations to provide a fundamental basis for understanding heterogeneous electrochemical reactions. Our GCP-K formulation arises naturally from minimizing the free energy using a Legendre transform relating the net charge of the system and the applied voltage. Performing this macroscopic transformation explicitly allows us to make the connection of GCP-K to the traditional Butler-Volmer kinetics. Using this GCP-K based free energy, we show how to predict both the potential and pH dependent chemistry for a specific example, the hydrogen evolution reaction (HER) at a sulfur vacancy on the basal plane of MoS_2. We find that the rate determining steps in both acidic and basic conditions are the Volmer reaction in which the second hydrogen atom is adsorbed from the solution. Using the our GCP-K formulation, we show that the stretched bond distances change continuously as a function of the applied potential. This shows that the main reason for the higher activity in basic conditions is that the transition state is closer to the product, which leads to a more favorable Tafel slope of 60mV/dec. In contrast if the transition state were closer to the reactant, where the transfer coefficient is less than 0.5 we would obtain a Tafel slope of almost 150mV/dec. Based on this detailed understanding of the reaction mechanism, we conclude that **the second hydrogen at the chalcogenide vacant site is the most active towards the hydrogen evolution reaction**. Using this as a descriptor, we compare to the other 2H group VI metal dichalcogenides and predict that vacancies on **$MoTe_2$ will have the best performance towards HER.**

1. Introduction

The field of heterogeneous electrochemistry has been growing rapidly, particularly with a focus on electrochemical water splitting and CO_2 reduction to efficiently convert electrical energy generated from traditional and renewable energy sources to recyclable energy carriers like H_2 or carbon based fuels[1-4]. Simultaneously, advances in Quantum Mechanics (QM) based methods now enable the detailed reaction mechanisms to be determined for simple low index models of the catalytic surfaces[5]. Electrocatalysis is driven by applying a voltage across the reaction cell, providing a sensitive control of the rate not available with traditional heterogeneous thermal catalysis in which only the temperature and pressure can be used to drive the chemical reactions. Recently we have developed modifications in the traditional QM (fixed numbers of electrons) to enable the applied voltage (U) to be fixed, Grand Canonical QM (GC-QM)[6]. In GC-QM, the charges change continuously during the electrochemical reaction to keep the applied U constant. This provides a new way (Grand Canonical Potential Kinetics, GCP-K) to understand the kinetics, completely different from the traditional Butler-Volmer description of electrochemistry in which the potential surface is followed for each species keeping an integer number of electrons, from which the system can transform to a product state by tunneling between the electrode and the reacting molecule. This is illustrated in Figure 1.

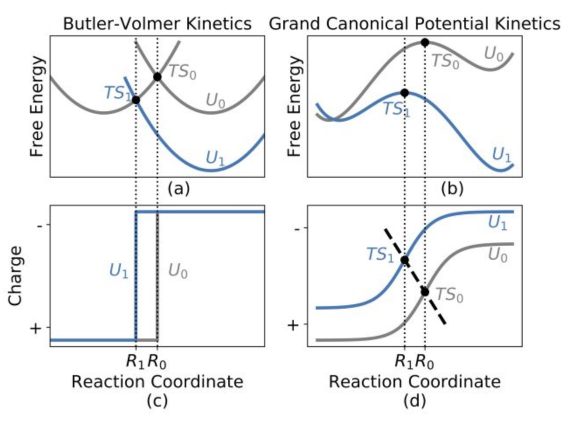

Figure 1. Schematic showing how voltage dependent electrochemical reactions described by grand canonical potential kinetics (GCP-K). (b) and (d) differs from the more standard view of Butler-Volmer kinetics (a) and (c). As the voltage is changed from U_0 to U_1, the energy profiles shift as in (a) and (b), while the relevant reaction coordinate changes from R_0 to R_1. The Butler-Volmer picture in (c) can be considered as a special case of the GCP-K scheme (d) in which the electron transfers instantaneously.

Although the voltage dependent grand canonical potential can be obtained from quantum mechanical calculations, the connection to the Butler-Volmer kinetics is non-trivial as the latter theory is formulated for integer-charged solvated molecules. In this paper, we provide a macroscopic theoretical foundation for a new understanding of heterogeneous electrochemistry based on GPC-K and compare it to the traditional Butler-Volmer description.

Particularly, we will show that the voltage-dependent grand canonical potential (GCP) for surface states can be derived from traditional fixed-electron based free energies by using a Legendre transformation. As a result, we find that GCP depends quadratically on the applied potential U and on the number of electrons allowing a continuous description of the evolution of the reaction intermediates and transition states.

To illustrate the concepts underlying this new theoretical formulation, we applied the GCP-K to study the detailed reaction mechanism for the hydrogen evolution reaction (HER) on the basal plane of MoS_2. Over the past decade, many theoretical and experimental studies have shown that MoS_2 and other transition metal dichalcogenides can produce hydrogen gas efficiently[7-8]. Initially it was believed that hydrogen atom adsorption energy on the edge sulfur (S-H bond) provided the most active site[9-10]. However, our QM study of the HER mechanism[11] showed that the rate determining step (RDS) for dihydrogen formation at edge sites takes place via the Heyrovsky reaction in which a hydrogen (proton) from the solution (H_3O+) reacts with the Mo−H metal hydride bond at the edge to form H_2. The S−H bonded site is not a kinetically important intermediate.

In addition to the edges of MoS_2, the HER has been studied extensively for other reactive sites. This includes the 1T phase of MoS_2[12,13] and amorphous MoS_x[14-17]. Activating the basal plane of MoS_2 is of interest because of the potentially abundant number of active sites. Early studies showed that the untreated basal plane performs some HER catalysis, but the performance is less favorable than the edge sites[18-21]. Later, it was found that artificially creating sulfur vacancies using Ar plasma showed a correlation between the number of vacant sites and HER activity[22]. However, the experimental conclusion of this study is controversial, since others showed that the creation of sulfur vacancy by plasma is *not* responsible for the HER[23]. Later it was found that under electrochemical conditions sulfur vacancies are created without the use of Ar plasma[24]. However, the interpretation is complicated because the observed reactivity might arise also from the presence of edge sites since they are known to be active towards HER. This complicates the experimental identification of the true nature of the active sites. Thus, although many studies have been performed to optimize the basal plane for HER, the reaction mechanism is not yet established.

In this study, we performed QM calculations using our new grand canonical potential (GCP-K) formulation to determine as a function of applied potential the reaction steps involved in HER at sulfur vacancies on the basal plane of MoS_2. By accounting for all HER related chemical processes, we predict the Tafel plots and onset potentials in both the acidic and basic conditions.

Particularly, we resolved the difference in activity between the acidic and basic conditions[25]. We focus the detailed discussions on MoS_2, but we report the results for these new methods applied to the other transition metal dichalcogenides having the 2H structure, predicting that $MoTe_2$ is the best and MoS_2 is the worst for HER via basal plane vacancies.

In contrast to the simplistic view in which the performance descriptor is protonation of the reactive site, we find that it is the addition of the second hydrogen to the reactive site that is the important step. Indeed, this Volmer step determines the reaction rates in both acidic and basic conditions. Thus we conclude that **the adsorption energy of the second hydrogen atom can be used as the proper descriptor** to assess performance for the class of group VI transition metal dichalcogenides.

2. The Grand Canonical Potential (GCP) formulation using the constant charge condition

Quantum mechanics (QM) calculations, such as density functional theory (DFT), are nearly always performed with a **fixed number of electrons**. To appropriately account for electrochemical conditions at a specified applied voltage, we must modify the methodology for the QM. Early methods to correct the QM for electrochemical systems obtained a relationship between the number of electrons and the work function of the slab surface, where surface coverage[26], explicit ions, or uniform background charges[27,28] were introduced to modulate the work function of the system. Later it was found that counter ions can be included in the implicit solvation model to provide a combined solvent-slab free energy, where the corresponding grand canonical potential is defined as in (1) so that electrochemistry processes can be obtained directly using $G(n; U)$[29-31].

$$G(n;U) = F(n) - ne(U_{SHE} - U) \tag{1}$$

where G is the grand canonical free energy, which depends on the applied voltage U vs. SHE, n is the number of electrons, e is unit electron volt in energy, F is the total free energy as a function of n, and $U_{SHE} = \mu_{e,SHE}/e$ is the electronic energy at the standard hydrogen electrode (SHE) condition. The signs are chosen such that U is directly related to the experimentally defined value, i.e., U=−0.1V corresponds to −0.1V vs. SHE. Changing to the reference hydrogen electrode (RHE) shifts the reference fermi level further depending on the pH of the solution.

However, for $G(n; U)$ to be used as a thermodynamic potential, the number of electrons in the system must be equilibrated to the applied voltage. To do this the QM self-consistent approach is to match the electronic fermi level to that of the applied potential by changing the occupation of the electronic bands, thus varying the number of electrons[32-33]. Mathematically, this is

$$\mu_e = \frac{dF(n)}{dn} = e(U_{SHE} - U) \text{ or } \frac{dG(n;U)}{dn} = 0 \tag{2}$$

Thus, we *define* the macroscopic thermodynamic **Grand Canonical Potential** (GCP) as in (3).

$$\mathrm{GCP}(U) = \min_{n} G(n;U) = \min_{n} \left(F(n) - ne(U_{SHE} - U)\right) \tag{3}$$

Since experimental observations typically involve the response of a chemical system as a function of the applied voltage, we recommend using GCP(U) directly as an explicit function of U in QM calculations modeling electrochemical processes. In contrast many recent studies *have assumed* a GCP(U) that *depends linearly on U* [34-35].

Instead, our definition of the GCP(U) in the form of minimization as in equation (3), makes it immediately obvious that *the linear approximation is not correct*. **The form of $F(n)$ must be at least quadratic in n** in order to describe the minimization of GCP(n; U). As reported previously[27-28], the form of GCP(U) is in fact approximately quadratic. Hence, we expand $F(n)$ in a quadratic form

$$F(n) = a(n - n_0)^2 + b(n - n_0) + c,$$

where a, b and c are fitted parameters. Substituting and performing the minimization, we have

$$\mathrm{GCP}(U) = -\frac{1}{4a}(b - \mu_{e,\mathrm{SHE}} + eU)^2 + c - n_0\mu_{e,SHE} + n_0 eU \qquad (4)$$

Using this form, we relate the parameters a, b, and c to physical quantities as follows.

- First, when the system is neutral, $F(n = n_0) = c$.
- Second, the number of electrons is $n(U) = -\frac{1}{e}\frac{\partial GCP(U)}{\partial U} = n_0 - \frac{1}{2ae}(b - \mu_{e,\mathrm{SHE}} + eU)$. Thus at the potential of zero charge, $n(U_{\mathrm{PZC}})=n_0$, and we obtain $b = \mu_{e,\mathrm{SHE}} - eU_{\mathrm{PZC}}$.
- Finally, the differential capacitance is $C_{\mathrm{diff}} = \frac{\partial n}{\partial U} = -\frac{1}{2a}$, which gives $a = -\frac{1}{2C_{\mathrm{diff}}}$.

Summarizing, the grand canonical potential and the free energy have the following form in terms of physical quantities:

$$\mathrm{GCP}(U) = \frac{e^2 C_{\mathrm{diff}}}{2}(U - U_{\mathrm{PZC}})^2 + n_0 eU + F_0 - n_0\mu_{e,SHE} \qquad (5a)$$

$$F(n) = -\frac{1}{2C_{\mathrm{diff}}}(n - n_0)^2 + (\mu_{e,SHE} - eU_{\mathrm{PZC}})(n - n_0) + F_0 \qquad (5b)$$

where

- C_{diff} is the differential capacitance, calculated from parameter a
- U_{PZC} is the potential of zero net charge, calculated from parameter b
- F_0 is the free energy at zero net charge, calculated from parameter c
- n_0 is the number of electrons at zero net charge, summing all valence electrons in the QM
- $\mu_{e,\mathrm{SHE}}$ is the chemical potential of an electron vs. SHE
- e is the energy of an electron volt, which is for unit conversion from voltage to energy

The quadratic dependence in the free energy $F(n)$ and the grand canonical potential GCP(U) implies that the capacitive effects will participate in the electrochemical processes. Fundamentally, this is due to the fact that heterogeneous systems allow electrons to delocalize into broad electronic bands, resulting in fractional occupations. Thus, the number of electrons can be vary continuously, leading to the capacitive contributions.

We note that a similar quadratic form

$$G(U) = F(n(U)) - ne(U_{\mathrm{SHE}} - U)$$

was proposed previously[36], but the relationship between n and U was established via the work function rather than a proper thermodynamic minimization.

Our approach shows that the work function is not needed to calculate the grand canonical potential since we define GCP(U) rigorously from the free energy $F(n)$ via a Legendre transform. Using the Legendre transform allows us to write $F(n)$ and GCP(U) in terms of physical parameters, with the connection to Butler-Volmer kinetics as discussed below.

3. Simulation Model for the Basal Plane of MoS_2

To predict the QM properties of a sulfur vacancy on the basal plane of MoS_2, we used a 3x3 MoS_2 periodic slab. Removing a sulfur atom exposes three molybdenum atoms that become available for bonding. This leads to four possible intermediate states with 0 to 3 hydrogen atoms at the vacant site. We label them as **0**, **1**, **2** and **3** or [MoS_2], [MoS_2]H, [MoS_2]H_2 and [MoS_2]H_3 in Figure 2. Detailed description of the quantum mechanical calculations is provided in the supplementary information.

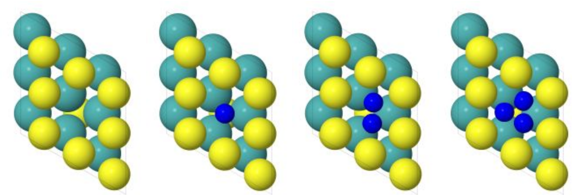

0 [MoS_2] **1** [MoS_2]H **2** [MoS_2]H_2 **3** [MoS_2]H_3

Figure 2. Four possible states for Hydrogen adsorption at the sulfur vacancy site. Blue: hydrogen atom; yellow: sulfur atom; cyan: molybdenum atom.

To illustrate the quadratic behavior of the grand canonical potential, we examined the voltage dependence for [MoS_2]H in detail. [MoS_2]H is used here because we find below that it is both the most stable intermediate thermodynamically and most populous for the steady state reaction. Figure 3(a) shows that the solvated free energy $F(n)$ as a function of accumulated charges *appears* to be linear. However, this is due to the large contribution from the free energy of an electron at SHE. Rearranging Equation (5), leads to (6),

$$F(n) - \mu_{e,SHE}n = -\frac{1}{2C_{\mathrm{diff}}}(n - n_0)^2 - \mu_{e,SHE}n_0 - eU_{\mathrm{PZC}}(n - n_0) + F_0 \qquad (6)$$

Equation (6) reveals the quadratic dependence on charge, as shown in Figure 3(b). We see that the minimum is approximately at $n=n_0$.

Under electrochemical conditions, a nonzero voltage, U, is applied to drive the reaction. This shifts the free energy in equation (6) by neU, leading to $G(n, U)$, as defined in Equation (1). Figure 3(c) shows that applying a voltage of $U=-0.5$V vs. SHE shifts the minimum of $G(n; U)$ towards more electrons, indicating that the slab becomes more negatively charged.

Thus, although the free energy $F(n)$ appears to be linear in Fig. 3a, the thermodynamically relevant potential $G(n; U)$ or GCP(U) in Fig. 3c is clearly quadratic.

4. Relationship between grand canonical potential reaction kinetics and Butler-Volmer reaction kinetics

The above formulation can be used for stable states because the equilibrium geometries usually change little as the applied potential changes. However, since the transition state (TS) is the maximum along the *minimum energy path* (MEP) for the reaction coordinate, *the TS geometry will change as the applied voltage changes.*

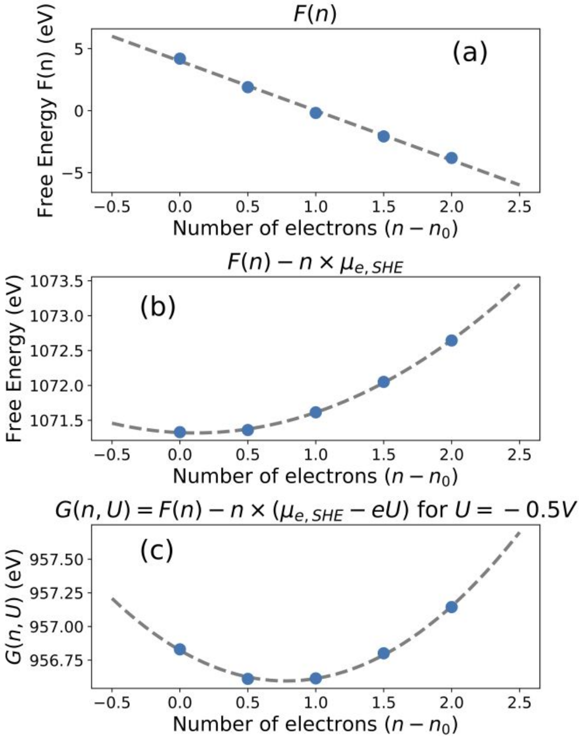

Figure 3. the free energy and grand canonical potential as a function of the number of electrons. The DFT energies are indicated by Blue dots, the dashed curve is the polynomial fit. (a) a linearly fit to $F(n)$, (b) a quadratic fit to $F(n) - n \times \mu_{e,\mathrm{SHE}}$, (c) a quadratic fit GCP(n, U).

Fig 1 (b) shows schematically that as the voltage is changed from U_0 to a more negative U_1, the negatively charged product becomes more stable, shifting the potential energy surface downward for the species. However, this energy energy changes as the geometries change along the MEP. Because the reactant has fewer electrons, the stabilization is less effective, resulting in a leftward shift of the transition state towards the reactant. The coordinate along the reaction coordinate changes from R_0 to R_1 in Figure 1(b). In comparison, for Butler-Volmer kinetics[37-39], only two states are involved, and the shift from R_0 to R_1 is the result of the shift in energy for the final state, as shown in Figure 1(a).

The difference between the *grand canonical potential reaction kinetics* (GCP-K) and Butler-Volmer kinetics is more obvious for the reaction path in the charge-reaction coordinate or (n, R) plane as shown in Figure 1(c) and 1(d). In the Bulter-Volmer picture, an electron is transferred through tunneling from the electrode to the product, resulting in a discontinuity in the (n, R) plane. However, in extended systems where intermediates are adsorbed on the surface, there can be fractional charges per unit area since electrons are delocalized. As a result, the surface species can charge or discharge continuously, leading to a smooth reaction path in the (n, R) plane, as shown in Figure 1(d). Thus, the Bulter-Volmer picture in the (n, R) plane can be considered as the special case of the GCP-K picture in which the electron transfer takes place *instantaneously* as in Figure 1(c).

In the GCP-K picture, the reaction path changes continuously in the (n, R) plane. Thus, both the *charge n* and the *spatial reaction coordinate R* are relevant coordinates. Because the constant charge free energy $F(n)$ is used to transform to GCP(U), we must prove that the grand canonical potential for the transition state obtained from the constant charge $F(n)$ coincides with the grand canonical potential obtained from constant voltage calculations.

The transition state grand canonical potential $\mathrm{GCP}_{\mathrm{TS,n}}(U)$ can be found explicitly by transforming $F_{\mathrm{TS}}(n)$, where $F_{\mathrm{TS}}(n)$ is the barrier for each fixed charge n such that

$$F_{\mathrm{TS}}(n)=\max_R F(n,R), \text{ with } R_{\mathrm{IS}} < R < R_{\mathrm{FS}}$$

Then,

$$\mathrm{GCP}_{\mathrm{TS,n}}(U) = \min_R(F_{\mathrm{TS}}(n) - ne(U_{\mathrm{SHE}} - U))$$

On the other hand, including the spatial dependence in Equation (1), leads to

$$G(n, R; U) = F(n, R) - ne(U_{\mathrm{SHE}} - U)$$

Thus, the barrier calculated from the explicit voltage dependent grand canonical potential is defined as

$$\mathrm{GCP}_{\mathrm{TS,U}}(U) = \max_{\mathrm{R}}\mathrm{GCP}(U, R) = \max_{\mathrm{R}}\min_{\mathrm{n}}\mathrm{GCP}(n, R; U)$$

To show that the two approaches, $\mathrm{GCP}_{\mathrm{TS,U}}(U)$ and $\mathrm{GCP}_{\mathrm{TS,n}}(U)$, are equivalent, we employ the minimax theorem[40]:

Given:

1. $F(n, R)$ is quadratic and thus convex in n, then so is $\mathrm{GCP}(n, R; U) = F(n, R) - ne(U_{\mathrm{SHE}} - U)$,
2. The reaction path is smooth in extended systems since the charges transfer continuously at the electrode. By the definition of the transition state, the reaction path is concave in R in the neighborhood of R_{TS}.

Then,

$$\begin{aligned} \mathrm{GCP}_{\mathrm{TS,U}}(U) &= \max_R \min_n (\mathrm{GCP}(n, R; U)) \\ &= \min_n \max_R (\mathrm{GCP}(n, R; U)) \\ &= \min_n \max_R \left(F(n, R) - ne\left(U_{SHE} - U\right)\right) \\ &= \min_n \left(F_{\mathrm{TS}}(n) - ne\left(U_{SHE} - U\right)\right) \\ &= \mathrm{GCP}_{TS,n}(U) \end{aligned}$$

Thus, the *transition state obtained from the constant charge barriers and the constant voltage barriers are indeed equivalent*. This relationship allows us to calculate the barriers for a system with a fixed number of electrons (standard QM) and then use the Legendre transform to obtain the voltage dependence for the transition state. Figure 1(d) shows that for each voltage (U), there corresponds a transition state with a specific charge (n) and spatial distance (R_{TS}). Thus, R_{TS} is a function of charge (n), or $R_{\mathrm{TS}}(n) = \mathrm{argmax}_R F(n, R)$.

Because the grand canonical potential of the transition state is found by minimization in n and maximization in R, then at the transition state we have

$$\frac{d}{dR}\frac{d}{dn}\mathrm{GCP}(n,R;U)=0 \tag{7}$$

As discussed above, GCP(n, R; U) depends on R and U quadratically around the transition state, the derivatives in n and R reduce the dependence from order 2 to order 1. As the result, Equation (7) implies that $R_{TS}(n)$ *depends linearly on n*. This linear dependence is shown qualitatively as the dashed line in Figure 1(d).

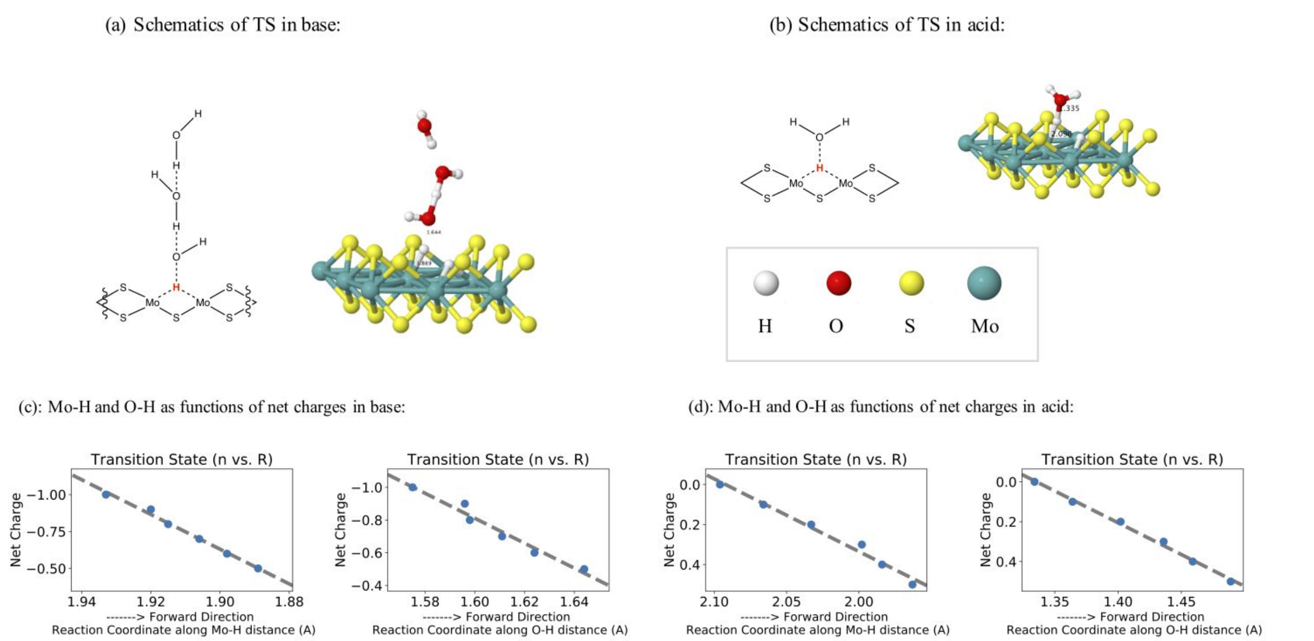

Figure 4. The transition states as the system evolves from $[MoS_2]H$ to $[MoS_2]H_2$. (a): the transition state structure in basic conditions. (b): the transition state structure in acidic conditions. (c): relationships between the transition state charge (n) and spatial coordinates (R_{TS}) in basic conditions. (d): relationships between the transition state charge (n) and spatial coordinates (R_{TS}) in acidic conditions. The linear relationships in (c) and (d) agree with the qualitative picture in Figure 1(d).

To show this linear relationship quantitatively, we studied the transition state of hydrogen transfer from the solution to $[MoS_2]H$ to produce $[MoS_2]H_2$, as shown in Figure 4. We show below that this is the rate determining step (RDS) for HER at the sulfur vacancy site on the basal plane of MoS_2. In this primary step, the hydrogen atom gradually moves from the oxygen atom of the water molecule towards the molybdenum atom at the reaction center. As a result, two spatial coordinates are important. One is the Mo−H distance and the other is O−H distance, such that in the forward direction, the distance of Mo−H is becoming shorter and the distance of O−H is becoming longer. Fig 4 (e)-(h) shows that the relationship between R and n for the transition state is linear as predicted by the GPC-K approach.

5. Discussion of the HER mechanism on MoS_2 basal plane

5.1The Hydrogen Evolution Reaction in Acidic Conditions

Using the information from Fig. 5, we can calculate the grand canonical potential of all the relevant intermediates and their connecting transition states at any given applied potentials. In this reaction, the sulfur vacancy site can bind up to three hydrogen atoms.

- At U=−500mV, the most stable state is **1**, or $[MoS_2]H$.
- However, at a more negative potential, U=−700mV, the most stable state becomes **2**, or $[MoS_2]H_2$.

This is expected because the grand potential G(n, U) = F(n) – neU is smaller for more negative charge (larger n) when a negative potential (more negative U) is applied. Thus the $[MoS_2]H_2$ becomes more stable than $[MoS_2]H$ with a more negative charge.

5.1a start with the sulfur vacant site with no hydrogen atom adsorbed:

- At U= −500mV we first adsorb a hydrogen atom from the solution at **TS01** with a barrier of 1.7 kcal/mol
- At U= −700mV we first adsorb a hydrogen atom from the solution at **TS01** with a barrier of and 0.8 kcal/mol.

5.1b Start with one hydrogen atom adsorbed at the site:

This site can react with another hydrogen from the solution to *generate an* H_2, while leaving behind the empty site with

- A barrier (**TS10**) of 22.6 kcal/mol at U=−500 mV and
- A barrier (**TS10**) of 20.3 kcal/mol at U=−700 mV

Or it can abstract a second hydrogen from the solution to form $[MoS_2]H_2$ with

- A barrier of 15.3 kcal/mol (**TS12**) at U=−500 mV and
- A barrier of 13.6 kcal/mol (**TS12**) at U=−700 mV

5.1c Start with two hydrogen atoms adsorbed at the site:

They can react with each other to *generate an* H_2 while leaving behind the empty site with

- A barrier (**TS20**) of 17.9 kcal/mol at U=−500 mV and
- A barrier (**TS20**) of 18.2 kcal/mol at U=−700 mV

or one of the hydrogen atoms can react with another hydrogen atom from water to generate H_2 while leaving behind $[MoS_2]H$ with

- A barrier of 8.8 kcal/mol at U=−500 mV (**TS21**). and
- A barrier of 7.5 kcal/mol at U=−700 mV (**TS21**).

or $[MoS_2]H_2$ can abstract another hydrogen solution to form $[MoS_2]H_3$ via **TS23**. However, we found that this step involves the same transition state as **TS21**, thus the barriers

This shows that at high applied potential, there is a bias toward the intermediate species with more electrons, making them more stable.

5.2a Start with no hydrogen adsorbed:

- At U = −500mV, the barrier **TS01** leading to $[MoS_2]H$ is very low at 3.3 kcal/mol,
- At U = −700mV, **TS01** is even lower at 2.4 kcal/mol.

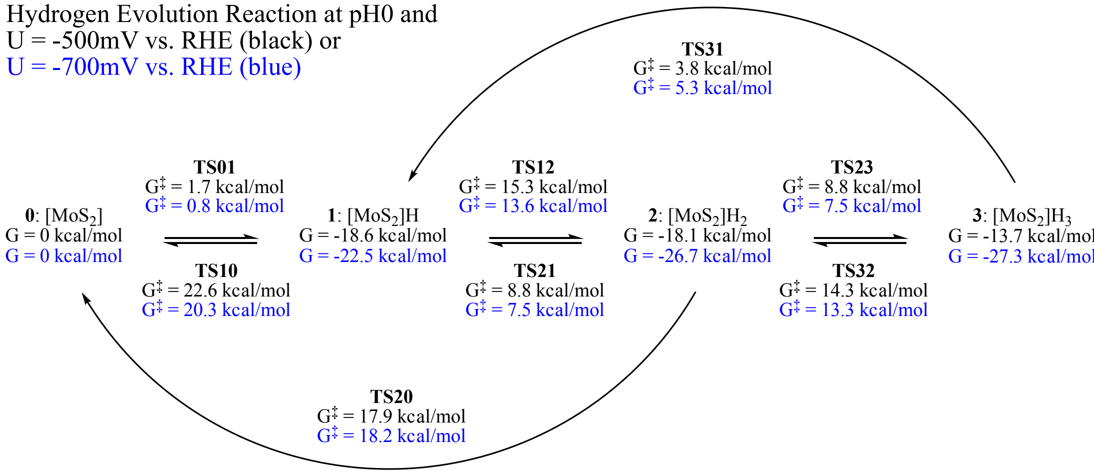

Figure 5. The Free energies at 298K under acid conditions for all reaction intermediates and transition states involved in the HER at the sulfur vacancy on the basal plane of MoS2. Black: U = −500mV vs RHE, blue: U = −700mV vs. RHE.

are 8.8 and 7.5 kcal/mol.

For $[MoS_2]H_3$, no more hydrogen can be added, thus it can generate H_2 via the Volmer step (**TS31**) with a barrier of 3.8 and 5.3 kcal/mol, or it can generate H_2 via the Heyrovsky step (**TS32**) with a barrier of 14.3 and 13.3 kcal/mol.

5.2 Hydrogen Evolution Reaction in Basic Conditions

Similarly, we can use the GCP-K method in basic conditions to calculate the GCP energy of each species and the barrier for each reaction. However, because we use RHE, the reference fermi energy of the electron is shifted by pH × 0.059 eV. As shown in Figure 6, at U = −500mV vs RHE, the relative stability of $[MoS_2]H$, $[MoS_2]H_2$ and $[MoS_2]H_3$ are very similar, while $[MoS_2]$, the state with no hydrogen atom adsorbed, is much less stable. Thus under basic conditions, we conclude that there is always at least a hydrogen atom adsorbed at the reaction site. Specifically,

- At U= −500 mV, the most stable state is **1**, or $[MoS_2]H$, same as the acidic case,
- At U= −700 mV, the most stable state is shifted to **3**, or $[MoS_2]H_3$.

Such a low barrier is due to the large thermodynamic force, so that $[MoS_2]H$ is −15.9 and −19.5 kcal/mol downhill from $[MoS_2]$ for −500mV and −700mV, respectively. However, the kinetics at $[MoS_2]H$ is more unfavorable because it is relatively too stable. It has to overcome a large thermodynamic force to react with another water molecule to form H_2 and $[MoS_2]$ via **TS10**.

5.2b Start with one hydrogen atom adsorbed:

Different from the vacant state $[MoS_2]$, the kinetics at $[MoS_2]H$ is more unfavorable because it is relatively much more stable. To react with another water molecule to form H_2 and $[MoS_2]$ via **TS10**, it has to overcome a large thermodynamic force:

- At U = −500mV, the barrier **TS10** leading to $[MoS_2]$ is 28.8 kcal/mol,
- At U = −700mV, the barrier **TS10** is 27.1 kcal/mol.

On the other hand, it is much easier to form two adsorbed hydrogen atoms at the reaction site (**TS12**), since $[MoS_2]H_2$ is similar in energy to $[MoS_2]H$.

- A barrier (**TS12**) of 15.1 kcal/mol at U = −500mV,

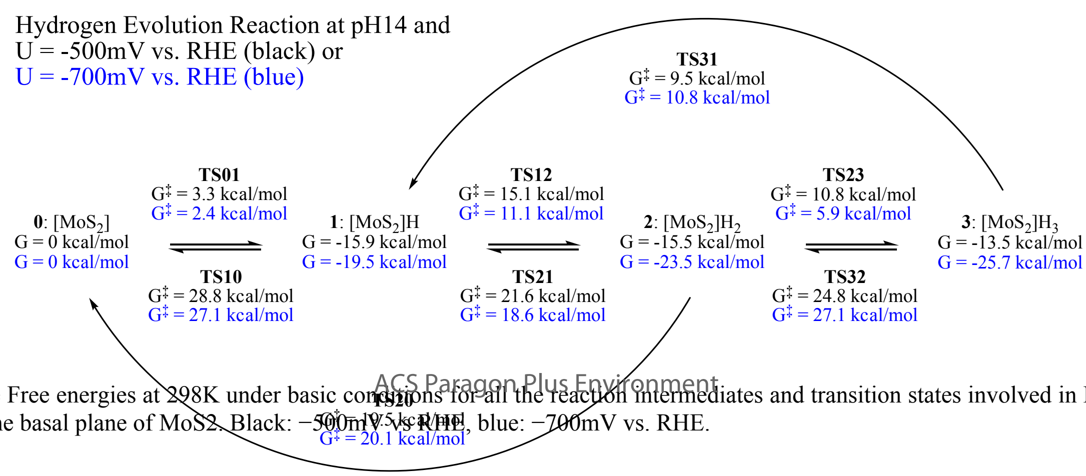

Figure 6. The Free energies at 298K under basic conditions for all the reaction intermediates and transition states involved in HER at the sulfur vacancy on the basal plane of MoS2. Black: −500mV vs RHE, blue: −700mV vs. RHE.

- A barrier (**TS12**) of 13.6 kcal/mol at U = −700mV.

5.2c Start with two hydrogen atoms adsorbed:

Having two adsorbed hydrogen atoms for $[MoS_2]H_2$ allows the H_2 molecule to be formed via the Heyrovsky mechanism (**TS21**) or the Tafel mechanism (**TS20**). However, both steps have to overcome a ~20kcal/mol barrier at −500mV and −700mV.

- At U = −500mV, the Tafel barrier (**TS20**) is 19.5 kcal/mol and the Heyrovsky barrier (**TS21**) is 21.6 kcal/mol,
- At U = −700mV, the Tafel barrier (**TS20**) is 20.1 kcal/mol and the Heyrovsky barrier (**TS21**) is 18.6 kcal/mol.

Instead of forming H_2 directly, $[MoS_2]H_2$ prefers to abstract one more hydrogen atom from the solution,

- A barrier (**TS23**) of 10.8 kcal/mol at U = −500mV,
- A barrier (**TS23**) of 5.9 kcal/mol at U = −700mV.

5.2d Start with three hydrogen atoms adsorbed:

At last, H_2 molecule can be formed from $[MoS_2]H_3$ via the Heyrovsky step (**TS32**) or the Tafel step (**TS31**). However, the Tafel step wins since the barrier is only 9.5 kcal/mol (−500mV) and 10.8 kcal/mol (−700mV), much lower than the activation energy for the Heyrovsky step with a barrier of almost 25 kcal/mol.

Summarizing, our analysis shows that hydrogen formation at the sulfur vacant site in basic conditions starts from $[MoS_2]H$, and continues to bind two hydrogen atoms sequentially, leading to $[MoS_2]H_3$. Then H_2 molecule is formed via the Tafel mechanism while $[MoS_2]H_3$ returns to the initial state $[MoS_2]H$.

6.0 Overall kinetics

Since all the energies of the relevant reaction intermediates and transition states are calculated as functions of applied potential using the quadratic grand canonical potential, the potential dependent rate constants are obtained using the Eyring rate equation. Once all rate constants are found, a microkinetic model is used to calculate the overall reaction rates and species concentrations.

First, we write the rate equations for all species as:

$$\frac{dx_0}{dt} = -k_{01}x_0 + k_{10}x_1 + k_{20}x_2$$

$$\frac{dx_1}{dt} = k_{01}x_0 - k_{10}x_1 - k_{12}x_1 + k_{21}x_2$$

$$\frac{dx_2}{dt} = k_{12}x_1 - k_{21}x_2 - k_{20}x_2 + k_{32}x_3$$

$$\frac{dx_3}{dt} = k_{23}x_2 - k_{32}x_3 - k_{31}x_3$$

and the Eyring rate equation as:

$$k_{ij}(U) = \frac{k_B T}{h}\exp\left(-\frac{\Delta G_{ij}^{\ddagger}(U)}{k_B T}\right)$$

where x_i is the concentration for each intermediate species, $k_{ij}(U)$ is the voltage dependent rate constant. However, the above set of equations is linearly dependent. We must include an additional constraint, $\sum_i x_i = 1$. If we are concerned only with the steady state chemistry, we can set the left hand sides of the above equation to zero. We then obtain the corresponding rates and concentrations by solving the system of linear equations. This then leads to the I-V plot and the Tafel plot as shown in Figure 7 (a) and (b).

Typically, experimental studies report the applied voltage at $10mA/cm^2$ as the onset potential for the catalyst. As shown in Figure 7(a), we found that the onset potential for the 11.1% sulfur vacancy to Mo atom ratio is −0.62V in acidic conditions, and −0.52V in basic conditions, agreeing qualitatively with experimental findings that the basal plane of MoS_2 is more active in basic conditions than in acidic conditions.

To correlate directly with experimental onset potentials, the experimental number density of the sulfur vacancies must be known. However, if the same sites are responsible for HER in both acidic and basic conditions, the onset potentials should scale linearly between acid and base. Indeed, exactly this linear relationship is found for all reported onset potentials for various samples[25], which are plotted in Figure 7(c). Our predicted onset potentials for base and acid are also plotted in figure 7c, which agree very well with our fitted line across the experimental samples. The Tafel slope in acidic condition is reported to be 127mV/dec, corresponding to a transfer coefficient of 0.47, which is similar to our predicted transfer coefficient of 0.39 derived from our Tafel slope of 155mV/dec in Figure 7(b). No Tafel slope has been reported for HER on the basal plane of MoS_2. We predict the Tafel slope to be 62 mV/dec.

As shown in Table 1, the dominant reaction intermediate is $[MoS_2]H$, the reaction site with one hydrogen atom adsorbed, agreeing with our discussions of Figure 5 and 6 where we conclude that $[MoS_2]H$ is the starting point of the catalytic cycle. Although the energetics of $[MoS_2]H$ is nearly identical

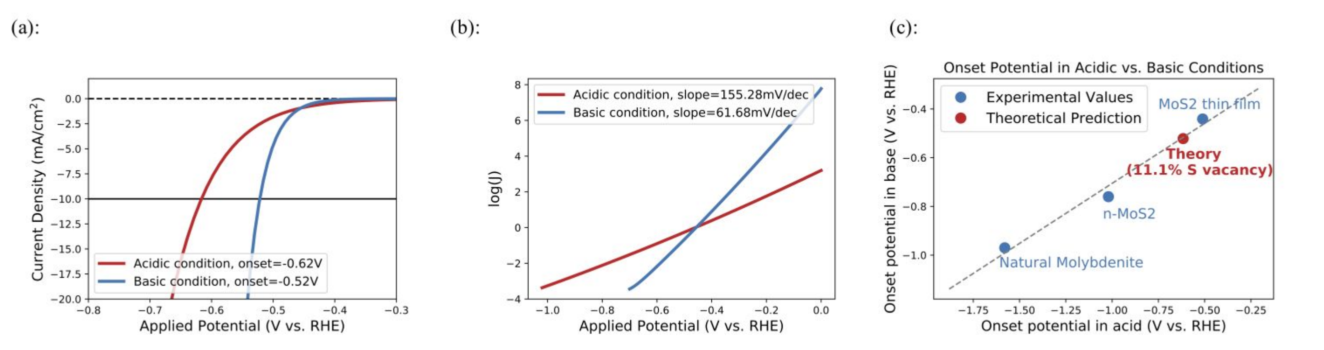

Figure 7. (a) QM predicted I-V curves for acidic and basic con-ditions. (b) Tafel plots for acidic and basic conditions. (c) Comparison between our QM predictions and the experimental interpolation from [A24]. This shows excellent agreement.

to $[MoS_2]H_2$, as shown in Figure 5 and 6, the near unity concentration is mainly the result of the rate determining step in which $[MoS_2]H$ is protonated to $[MoS_2]H_2$.

Condition	[MoS2]	[MoS2]H	[MoS2]H2	[MoS2]H3
Acidic (pH0)	0.0(−500mV)	0.9999	7.976×10^{-6}	1.119×10^{-9}
	0.0(−700mV)	0.9998	1.480×10^{-5}	2.544×10^{-7}
Basic (pH14)	0.0(-500mV)	0.9992	6.791×10^{-4}	7.323×10^{-5}
	0.0(-700mV)	0.6542	1.100×10^{-4}	0.3457

Table 1. Predicted species concentrations in fractions at the sulfur vacancy during hydrogen evolution reaction. The concentrations are normalized to sum to 1.

However, in basic condition, when the applied voltage is high, e.g., −700mV vs. RHE, the concentration of $[MoS_2]H_3$ increases to a nontrivial amount. This is mainly because the activation energy of the Tafel reaction (**TS31**) becomes e nearly as high as the original Volmer rate determining step of **TS12**.

7. Comparison with other Group VI Transition Metal Dichalcogendies

Since the adsorption of the second hydrogen atom to the sulfur vacant site is the general rate determining step, we can use its adsorption grand potential as the descriptor to compare the hydrogen evolution reaction activity at the basal plane across the class of group VI transition metal chalcogenides. The conventional adsorption energy is calculated at neutral charge, but since the number of electrons is not equilibrated to an applied voltage, this approach corresponds to intermediate states having different voltage. Such an approach is inappropriate for electrochemistry because the energy difference between two arbitrary voltages do not have any physical or chemical significance.

Instead, we compare the GCP of the intermediate species at the same voltage. We have also used the GCP approach to predict successfully the hydrogen adsorption energies at the same voltage (V=0 vs. SHE) to explain the hydrogen evolution relationships on $MoSSe/NiSe_2$[41] and FeP/NiP[42].

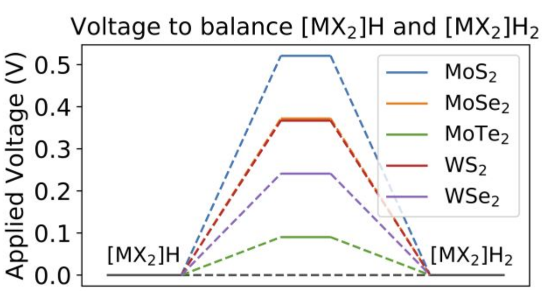

Figure 8. Required applied potential to obtain a zero reaction energy for the rate determining Volmer step from $[MX_2]H$ to $[MX_2]H_2$. We predict that this lowest required voltage will correspond to the best HER performance.

Since we have shown that the rate determining step is the Volmer reaction from $[MoS_2]H$ to $[MoS_2]H_2$, we can use the reaction energy of this step to compare the reactivity across materials with similar structures. However, the reaction energy, $\Delta G_{H2}(U) = G_2(U) - G_1(U)$ between **2** and **1**, depends on voltage. Instead of comparing $\Delta G_{H2}(U)$, we calculate the voltage necessary to obtain $\Delta G_{H2}(U)$=0, then the material with the lowest required voltage will be the most active towards HER. The corresponding voltages for different transition metal dichalcogenides are reported in the first numerical column in Table 2.

	Voltage when $G([MX_2]H) = G([MX_2]H_2)$	$\Delta G([MX_2])$	$\Delta G([MX_2]H_3)$
MoS2	η = 0.521V	0.82 eV	0.17 eV
MoSe2	η = 0.372V	0.83 eV	0.065 eV
MoTe2	η = 0.0902V	0.69 eV	0.046 eV
WS2	η = 0.367V	0.61 eV	0.26 eV
WSe2	η = 0.241V	0.65 eV	0.21 eV

Table 2. The relative grand canonical energies of $[MX_2]$ and $[MX_2]H_3$ at the optimal voltages. The relative energies $\Delta G([MX_2])$ and $\Delta G([MX_2]H_3)$ referenced to $[MX_2]H$ (or $[MX_2]H_2$) indicate whether the species might be important for the actual reaction mechanism.

In addition to the required potentials, we also calculated the relative energies of $[MX_2]$ and $[MX_2]H_3$ to determine whether they will interfere with the proposed stable states of $[MX_2]H$. As shown in Table 2, all of the relative energies of $[MX_2]$ are greater than 0.6 eV from the $[MX_2]H$ species, reaffirming that the vacant site $[MX_2]$ is not an important intermediate during HER at the basal plane. On the other hand, the $[MX_2]H_3$ are relatively much more stable, which allows the HER to proceed and complete the catalytic cycle from $[MX_2]H_3$ back to the original state of $[MX_2]H$.

Based on these calculations, we predict that $MoTe_2$ will have the best per site activity across the stable 2H group VI metal dichalcogenides, with η=0.09 V. Next is WSe_2 with η=0.24V, followed by WS_2 and $MoSe_2$ with η=0.37V, with MoS2 last at η=0.52V. Our predicted trend agrees with the observed trend[25] that for single crystal MoS_2 and $MoSe_2$, the onset potential for $MoSe_2$ is −0.78V vs. RHE in acidic condition, which is 0.47V lower than the onset potential of −1.25V vs. RHE for MoS_2. If a transfer coefficient of 0.5 is assumed, the onset potential of $MoTe_2$ will be 0.22V less negative than MoS_2 for the same density of chalcogenide vacancies.

8. Conclusion

In conclusion, we have shown that our formulations of the grand canonical potential kinetics (GCP-K) in terms of thermodynamics provides a fundamental basis for understanding electrochemical processes. Our GCP-K formulation arises naturally from minimizing the free energy using a Legendre transform. As the result, the free energies and the grand canonical potentials of the reaction intermediates include a quadratic term that depends on the differential capacitance C_{diff}. We use the minimax theorem to show that the barriers in the constant charge picture and constant potential picture describe the same transition states. Using this GCP based free energy, we showed how to predict both the potential and pH dependent chemistry of the hydrogen evolution reaction at the sulfur vacancy of the basal plane of MoS_2.

We find that the rate determining steps in both the acidic and basic are the Volmer reaction in which the second hydrogen forming is adsorbed from the solution. Using the our GCP formulation, we show that the stretched bond distances change continuously as a function of the applied potential. This shows that the main reason for the higher activity in basic conditions is that the transition state is closer to the product, leading to the much more favorable Tafel slope of 60mV/dec. In contrast if the transition state were closer to the reactant, where the transfer coefficient is less than 0.5 we obtain a Tafel slope of almost 150mV/dec.

Based on this detailed understanding of the reaction mechanism, we conclude that **the second hydrogen at the chalcogenide vacant site is the most active towards the hydrogen evolution reaction**. Using this as a descriptor, we compared the rest of the 2H group VI metal dichalcogenides and predict that **$MoTe_2$ will have the best performance towards HER among the 2H group VI transition metal dichalcogenides considered here.**

ASSOCIATED CONTENT

Supporting Information

The supporting information is available free of charge on the ACS Publications website. The supporting information includes the computational method, parameters for the potential dependent microkinetic model, and the computational structures used in this study.

AUTHOR INFORMATION

Corresponding Author

* wag@caltech.edu William A. Goddard III

ACKNOWLEDGMENT

This work was supported by the Joint Center for Artificial Photosynthesis, a DOE Energy Innovation Hub, supported through the Office of Science of the U.S. Department of Energy under Award Number DE-SC0004993. This work uses the resource of National Energy Research Scientific Computing center (NERSC).

REFERENCES

1. Walter, M. G., Warren, E. L., McKone, J. R., Boettcher, S. W., Mi, Q., Santori, E. A., Lewis, N. S. (2010). Solar water splitting cells. Chemical Reviews, 110(11), 6446–6473.
2. Roger, I., Shipman, M. A., Symes, M. D. (2017). Earth-abundant catalysts for electrochemical and photoelectrochemical water splitting. Nature Reviews Chemistry Volume 1, Article number: 0003.
3. Appel, A. M., Bercaw, J. E., Bocarsly, A. B., Dobbek, H., DuBois, D. L., Dupuis, M., Waldrop, G. L. (2013). Frontiers, Opportunities, and Challenges in Biochemical and Chemical Catalysis of CO 2 Fixation. Chemical Reviews, 113(8), 6621–6658.
4. Hori, Y. (2008). Electrochemical CO2 Reduction on Metal Electrodes. In Modern Aspects of Electrochemistry (pp. 89–189). New York, NY: Springer New York.
5. Nørskov, J. K., Bligaard, T., Rossmeisl, J., Christensen, C. H. (2009). Towards the computational design of solid catalysts. Nature Chemistry, 1(1), 37–46.
6. Sundararaman, R., Goddard, W. A., Arias, T. A. (2017). Grand canonical electronic density-functional theory: Algorithms and applications to electrochemistry. The Journal of Chemical Physics, 146(11), 114104.
7. Vesborg, P. C. K., Seger, B., Chorkendorff, I. (2015). Recent Development in Hydrogen Evolution Reaction Catalysts and Their Practical Implementation. The Journal of Physical Chemistry Letters, 951–957.
8. Yang, J., Shin, H. S. (2014). Recent advances in layered transition metal dichalcogenides for hydrogen evolution reaction. J. Mater. Chem. A, 2(17), 5979–5985.
9. Hinnemann, B., Moses, P. G., Bonde, J., Jørgensen, K. P., Nielsen, J. H., Horch, S., Nørskov, J. K. (2005). Biomimetic hydrogen evolution: MoS2 nanoparticles as catalyst for hydrogen evolution. Journal of the American Chemical Society, 127(15), 5308–5309.
10. Jaramillo, T., Jørgensen, K., Bonde, J. (2007). Identification of active edge sites for electrochemical H2 evolution from MoS2 nanocatalysts. Science, 317(5834), 100–102.
11. Huang, Y., Nielsen, R. J., Goddard, W. A., Soriaga, M. P. (2015). The Reaction Mechanism with Free Energy Barriers for Electrochemical Dihydrogen Evolution on MoS2. J. Am. Chem. Soc., 137 (20), pp 6692–6698.
12. Lukowski, M. A., Daniel, A. S., Meng, F., Forticaux, A., Li, L., Jin, S. (2013). Enhanced hydrogen evolution catalysis from chemically exfoliated metallic MoS2 nanosheets. Journal of the American Chemical Society, 135(28), 10274–10277.
13. Voiry, D., Salehi, M., Silva, R., Fujita, T., Chen, M., Asefa, T., … Chhowalla, M. (2013). Conducting MoS 2 Nanosheets as Catalysts for Hydrogen Evolution Reaction. Nano Letters, 13(12), 6222–6227.
14. Benck, J. D., Chen, Z., Kuritzky, L. Y., Forman, A. J., Jaramillo, T. F. (2012). Amorphous molybdenum sulfide catalysts for electrochemical hydrogen production: Insights into the origin of their catalytic activity. ACS Catalysis, 2(9), 1916–1923.
15. Morales-Guio, C. G., & Hu, X. (2014). Amorphous molybdenum sulfides as hydrogen evolution catalysts. Accounts of Chemical Research, 47(8), 2671–2681.
16. Li, Y., Yu, Y., Huang, Y., Nielsen, R. A., Goddard, W. A., Li, Y., Cao, L. (2015). Engineering the Composition and Crystallinity of Molybdenum Sulfide for High-Performance Electrocatalytic Hydrogen Evolution. ACS Catalysis, 5(1), 448–455.
17. Lassalle-Kaiser, B., Merki, D., Vrubel, H., Gul, S., Yachandra, V. K., Hu, X., Yano, J. (2015). Evidence from in situ X-ray absorption spectroscopy for the involvement of terminal disulfide in the reduction of protons by an amorphous molybdenum sulfide electrocatalyst. Journal of the American Chemical Society, 137(1), 314–321.
18. Tan, Y., Liu, P., Chen, L., Cong, W., Ito, Y., Han, J., Chen, M. W. (2014). Monolayer MoS 2 films supported by 3D nanoporous metals for high-efficiency electrocatalytic hydrogen production. Advanced Materials, 26(47), 8023–8028.
19. Li, H., Du, M., Mleczko, M. J., Koh, A. L., Nishi, Y., Pop, E., Zheng, X. (2016). Kinetic Study of Hydrogen Evolution Reaction over Strained MoS 2 with Sulfur Vacancies Using Scanning Electrochemical Microscopy. Journal of the American Chemical Society, 138(15), 5123–5129.
20. Zhang, J., Wu, J., Guo, H., Chen, W., Yuan, J., Martinez, U., Lou, J. (2017). Unveiling Active Sites for the Hydrogen Evolution Reaction on Monolayer MoS 2. Advanced Materials, 29(42), 1701955.
21. Gao, G., Sun, Q., Du, A. (2016). Activating catalytic inert basal plane of molybdenum disulfide to optimize hydrogen evolution activity via defect doping and strain engineering. Journal of Physical Chemistry C, 120(30), 16761–16766.
22. Li, H., Tsai, C., Koh, A. L., Cai, L., Contryman, A. W., Fragapane, A. H., Zheng, X. (2015). Activating and optimizing MoS2 basal planes for hydrogen evolution through the formation of strained sulphur vacancies. Nature Materials Volume 15, pages 48–53.
23. Li, G., Zhang, D., Qiao, Q., Yu, Y., Peterson, D., Zafar, A., Cao, L. (2016). All The Catalytic Active Sites of MoS 2 for Hydrogen Evolution. Journal of the American Chemical Society, 138(51), 16632–16638.
24. Tsai, C., Li, H., Park, S., Park, J., Han, H. S., Nørskov, J. K., Abild-Pedersen, F. (2017). Electrochemical generation of sulfur vacancies in the basal plane of MoS2 for hydrogen evolution. Nature Communications, 8, 1–8.
25. Wiensch, J. D., John, J., Velazquez, J. M., Torelli, D. A., Pieterick, A. P., McDowell, M. T., Lewis, N. S. (2017). Comparative

Study in Acidic and Alkaline Media of the Effects of pH and Crystallinity on the Hydrogen-Evolution Reaction on MoS 2 and MoSe 2. ACS Energy Letters, 2234–2238.

26. Skúlason, E., Karlberg, G. S., Rossmeisl, J., Bligaard, T., Greeley, J., Jónsson, H., Nørskov, J. K. (2007). Density functional theory calculations for the hydrogen evolution reaction in an electrochemical double layer on the Pt(111) electrode. Physical Chemistry Chemical Physics: PCCP, 9(25), 3241–3250.

27. Taylor, C. D., Neurock, M. (2005). Theoretical insights into the structure and reactivity of the aqueous/metal interface. Current Opinion in Solid State and Materials Science, 9(1–2), 49–65.

28. Taylor, C., Wasileski, S., Filhol, J.-S., Neurock, M. (2006). First principles reaction modeling of the electrochemical interface: Consideration and calculation of a tunable surface potential from atomic and electronic structure. Physical Review B, 73(16), 165402.

29. Jinnouchi, R., Anderson, A. B. (2008). Electronic structure calculations of liquid-solid interfaces: Combination of density functional theory and modified Poisson-Boltzmann theory. Physical Review B, 77(24), 245417.

30. Sha, Y., Yu, T. H., Merinov, B. V., Goddard, W. a. (2012). Prediction of the Dependence of the Fuel Cell Oxygen Reduction Reactions on Operating Voltage from DFT Calculations. The Journal of Physical Chemistry C, 116(10), 6166–6173.

31. Gunceler, D., Letchworth-Weaver, K., Sundararaman, R., Schwarz, K. a, Arias, T. a. (2013). The importance of nonlinear fluid response in joint density-functional theory studies of battery systems. Modelling and Simulation in Materials Science and Engineering, 21(7), 074005.

32. Sundararaman, R., Goddard, W. A. (2015). The charge-asymmetric nonlocally determined local-electric (CANDLE) solvation model. The Journal of Chemical Physics, 142(6), 064107.

33. Goodpaster, J. D., Bell, A. T., Head-Gordon, M. (2016). Identification of Possible Pathways for C-C Bond Formation during Electrochemical Reduction of CO2: New Theoretical Insights from an Improved Electrochemical Model. Journal of Physical Chemistry Letters, 7(8), 1471–1477.

34. Xiao, H., Cheng, T., Goddard, W. A.,Sundararaman, R. (2016). Mechanistic Explanation of the pH Dependence and Onset Potentials for Hydrocarbon Products from Electrochemical Reduction of CO on Cu (111). J. Am. Chem. Soc., 138 (2), pp 483–486.

35 Chan, K., Nørskov, J. K. (2016). Potential Dependence of Electrochemical Barriers from ab Initio Calculations. Journal of Physical Chemistry Letters, 7(9), 1686–1690.

36 Janik, M. J., Taylor, C. D., Neurock, M. (2009). First-Principles Analysis of the Initial Electroreduction Steps of Oxygen over Pt(111). Journal of The Electrochemical Society, 156(111), B126.

37. Morrison, S. R. (1980). Electrochemistry at Semiconductor and Oxidized Metal Electrodes, Springer U.S., Plenum Press, New York

38. Bard, A. J., Faulkner, L. R. (2001) Electrochemical Methods, John Wiley & Sons, New York

39. Sato, N. (1998), Electrochemistry at Metal and Semiconductor Electrodes., Elsevier Science B. V., Amsterdam, The Netherlands.

40. v. Neumann, J. (1928). Zur Theorie der Gesellschaftsspiele. Mathematische Annalen, 100(1), 295–320.

41. Zhou, H., Yu, F., Huang, Y., Sun, J., Zhu, Z., Nielsen, R. J., He, R., Bao, J., Goddard, W.A., Ren, Z. (2016). Efficient hydrogen evolution by ternary molybdenum sulfoselenide particles on self-standing porous nickel diselenide foam. Nature Communications, 7, 12765.

42. Yu, F., Zhou, H., Huang, Y., Sun, J., Qin, F., Bao, J., Goddard, W.A., Chen, S., Ren, Z. (2018). High-performance bifunctional porous non-noble metal phosphide catalyst for overall water splitting. Nature Communications, 9(1), 2551.

TOC graphic:

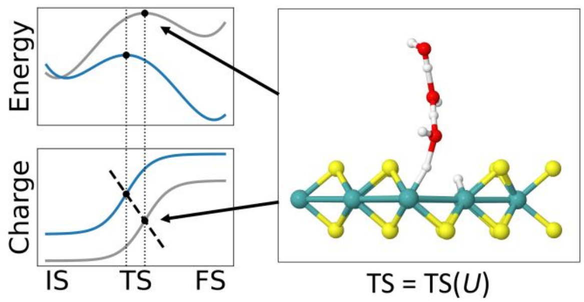

11